Comparison of Simulated Contrast Performance of Different Phase Induced Amplitude Apodization (PIAA) Coronagraph Configurations

Erkin Sidick*, Brian Kern, Andreas Kuhnert, and Stuart Shaklan
Jet Propulsion Laboratory, California Institute of Technology, 4800 Oak Grove Drive, Pasadena, CA 91109, USA

ABSTRACT

We compare the broadband contrast performances of several Phase Induced Amplitude Apodization (PIAA) coronagraph configurations through modeling and simulations. The basic optical design of the PIAA coronagraph is the same as NASA's High Contrast Imaging Testbed (HCIT) setup at the Jet Propulsion Laboratory (JPL). Using a deformable mirror and a broadband wavefront sensing and control algorithm, we create a "dark hole" in the broadband point-spread function (PSF) with an inner working angle (IWA) of $2(f\lambda/D)_{sky}$. We evaluate two systems in parallel. One is a perfect system having a design PIAA output amplitude and not having any wavefront error at its exit-pupil. The other is a realistic system having a design PIAA output amplitude and the measured residual wavefront error. We also investigate the effect of Lyot stops of various sizes when a postapodizer is and is not present. Our simulations show that the best 7.5%-broadband contrast value achievable with the current PIAA coronagraph is $\sim 1.5\times10^{-8}$.

Key words: Coronagraphy, adaptive optics, space telescopes, exoplanets

1. INTRODUCTION

One of the important milestones of the Phase Induced Amplitude Apodization (PIAA) coronagraph, one of NASA's High Contrast Imaging Testbed (HCIT) setups at the Jet Propulsion Laboratory (JPL), is to achieve 10^{-9} mean contrast in a dark hole with a 10% broadband light. So far a mean intensity of $5\text{x}10^{-10}$ has been achieved experimentally in a dark hole in the monochromatic point-spread function (PSF) with an IWA of $2(f\lambda/D)_{sky}$ using a configuration in which the DM was placed downstream of the front end PIAA set. The aspheric PIAA mirrors used in that experiment was made by Axsys and is identified as "PIAA1" in this paper. They are described in detail in Ref. 1. Placing the DM upstream of the front end PIAA sub-system enables the correction of high spatial frequencies before the PIAA remapping carries that information to frequencies higher than Nyquist frequency, allowing a larger outer working angle (OWA). Also, using an inverse-PIAA set at the back end enables one to recover a sharp diffraction-limited image over a useful field of view [2-3]. We compare the broadband-contrast performance of several PIAA coronagraph configurations through modeling and simulations. The structural design of the optical system as well as the parameters of various optical elements used in the analysis are drawn from those of the PIAA/HCIT system that have been implemented with one DM [4]. For the basic PIAA configuration currently implemented on the testbed, we investigate the effect of the residual phase error and its dispersion on the broadband contrast, examine the effect of Lyot stops of various sizes when a postapodizer is present, and compare the performances of three postapodizer designs. We also evaluate the effect of small PIAA output-postapodizer mismatch in terms of design and alignment.

2. BACKGROUND

2.1 Amplitude and Phase of the Exit-Pupil

The PIAA implementation on HCIT is described in detail in Ref. 5, so the description will not be repeated here. In order to simulate this testbed appropriately, the amplitude and the phase of the exit-pupil of the real system, without postapodizer and Lyot stop, were estimated. This was done by using the phase retrieval method described in Ref. 4 after a "flat-state" of the exit-pupil phase was reached by several iterations of wavefront control via phase retrieval and DM actuation. In this paper we mostly use the designed output amplitude of the PIAA1, but in several cases simulate the current testbed using the measured amplitude of the exit-pupil described in Ref. 4. The designed PIAA1 output

*Erkin.Sidick@jpl.nasa.gov; Phone 1 818 393-7585; Fax 1 818 393-9471; www.jpl.nasa.gov

amplitude is shown in an arbitrary gray-scale in Fig. 1(a). The residual measured exit-pupil phase error is shown as an Optical Path-Difference (OPD) map in Fig. 1(b). These amplitude and phase maps will serve as the starting point for the simulations in the next two sections. No other optical aberration is included in the simulations.

2.2 Occulter

The occulter is a binary mask having a shape as shown in Fig. 1(c). It is defined by the following five position quantities: $[R_{\min}, X_{\min}, X_{\max}, Y_{\min}, Y_{\max}] = [r_{\min}, x_{\min}, x_{\max}, y_{\min}, y_{\max}]/f$, where f is a focal length, $X_{\min}$ and $X_{\max}$ are the coordinates of the left and the right vertical flat sides, , $Y_{\min}$ and $Y_{\max} = -Y_{\min}$ are the coordinates of the top and the bottom flat sides, and $R_{\min}$ is the radius of the semi-circle. The occulter currently being used on the testbed has $[R_{\min}, X_{\min}, X_{\max}, Y_{\max}] = [1.46, 0.49, 3.24, 2.92](\lambda/D)_{\text{sky}}$, where the "sky" subscript denotes corresponding locations in the source plane. We will vary the values of $[X_{\max}, Y_{\max}]$ in this paper depending on the simulations to be performed, but keep the above values of $[R_{\min}, X_{\min}]$ as constants. Figure 1(c) shows a nominal occulter used in this paper and has $[X_{\max}, Y_{\max}] = [8.27, 7.94](\lambda/D)_{\text{sky}}$.

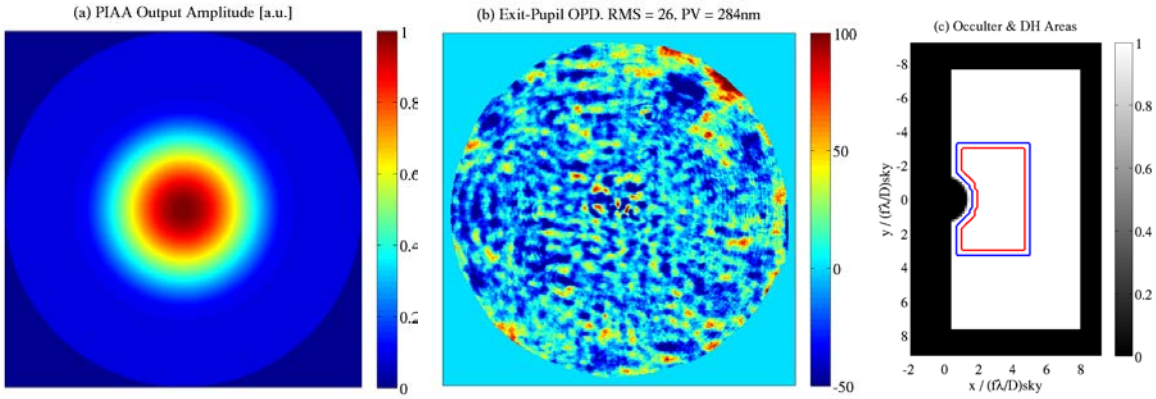

Fig.1. Designed amplitude (left) and estimated phase (center) at the exit-pupil, seen through the entire coronagraph with no occulter and Lyot stop. Both the amplitude and the phase are displayed in a linear scale. The amplitude at the edge is approximately 1/10 that at the center. This phase has been flattened by an iterative wavefront control process involving phase estimation and DM actuation before the data shown here were taken. The residual wavefront phase shown here is at spatial frequencies beyond the control of the DM. Its color-stretch is truncated in both ends for better visualization of its fine details. Also shown on the right is the occulter used in the simulations of this paper. It is a binary mask similar to the actual occulter in shape but with larger width and height. The blue and the red shapes inside the transparent area indicate the control and the contrast dark-hole areas, Ω_c and Ω_b, respectively.

2.3 Definitions of Dark-Hole Areas and Contrast

For the current optical system with only one DM, we carry out wavefront control (WFC) or electric-field conjugation (EFC) over a region Ω_c, where Ω_c is a half dark-hole region having the same shape as that of the occulter. The blue-frame in Fig. 1(c) shows the boundary of an example of Ω_c, and corresponds to $[R_{\min}, X_{\min}, X_{\max}, Y_{\max}] = [1.72, 0.75, 5.31, 3.44](\lambda/D)_{\text{sky}}$. We will evaluate the performance of the PIAA coronagraph using the mean normalized intensity, I_b, defined as

$$I_b = Mean\{I(x,y)/I_0\}_{(x,y)\in\Omega_b}, \quad (1)$$

where "Mean" represents a mean-value operation, $I(x,y)$ is the image intensity of the occulted star, I_0 is the peak value of the unocculted star intensity, and Ω_b represents the contrast dark-hole area. The subscript "b" means "big" and is used here to have the same naming convention as in our previous publications [6]. The red-frame in Fig. 1(c) shows the boundary of the Ω_b corresponding to the Ω_c in the same plot (blue-frame), and is defined by $[R_{\min}, X_{\min}, X_{\max}, Y_{\max}] = [2.04, 1.07, 4.99, 3.12](\lambda/D)_{\text{sky}}$. That is, we have chosen an Ω_b slightly smaller than the corresponding Ω_c in this study. We will keep the values of $[R_{\min}, X_{\min}]$ unchanged for both Ω_c and Ω_b in this report.

2.4 About the Wavefront Control (WFC) Algorithm

In this paper, we use a control algorithm similar to the "minimum-wavefront and optimal control compensator" described in detail in Ref. 7. This approach is also called "Actuator regularization" [8]. The WFC algorithm described in Ref. 7 uses the wavefront at the system exit pupil as its input, and calculate the actuator commands as its output. In the present case we set the DM actuators to superpose the negative of the electric-field (e-field) onto the image plane, with a goal to make the image intensity zero on the region Ω_c on the image plane. Therefore, the WFC algorithm uses an e-field column-vector $\vec{\mathbf{e}}$ as its input, where

$$\vec{\mathbf{e}} = \begin{bmatrix} \Re(\vec{\mathbf{E}}) \\ \Im(\vec{\mathbf{E}}) \end{bmatrix}. \tag{2}$$

The joint cost function now becomes as

$$J = \frac{1}{2}\left(\vec{\mathbf{e}}^T\vec{\mathbf{e}} + \gamma_{wu}\vec{\mathbf{u}}^T\vec{\mathbf{u}}\right), \tag{3}$$

and the gain matrix $\widetilde{\mathbf{G}}$ is obtained from

$$\widetilde{\mathbf{G}} = \left[\widetilde{\mathbf{S}}^T\widetilde{\mathbf{S}} + \gamma_{wu}\widetilde{\mathbf{I}}\right]^{-1}\widetilde{\mathbf{S}}^T, \tag{4}$$

where $\widetilde{\mathbf{I}}$ is an identity matrix and $\vec{\mathbf{u}}$ is the DM actuator command vector to be determined. It is obtained from $\vec{\mathbf{u}} = -\widetilde{\mathbf{G}}\vec{\mathbf{e}}_{test}$, where $\vec{\mathbf{e}}_{test}$ is the vector of the e-field to be minimized. In Eq. (2), $\vec{\mathbf{E}}$ is the column-vector of the complex e-field on region Ω_c. It is formed by stacking the elements of the complex e-field on region Ω_c in a certain order, as was explained in Eq. (1) of Ref. 7. The $\Re(\vec{\mathbf{E}})$ and the $\Im(\vec{\mathbf{E}})$ are the real and the imaginary parts of $\vec{\mathbf{E}}$, respectively. In Eq. (4), the $\widetilde{\mathbf{S}}$ is the sensitivity matrix consisting of the influence functions of all actuators, and γ_{wu} is the actuator regularization factor. Our Fast Fourier-Transform (FFT) based simulation tool calculates the complex e-field at the final focal plane directly. Therefore, the e-field estimation step [8] is not needed in our simulations. The simulation creates a 1103x1103 pixels (pix) PSF image in the final focal plane, with ~0.987pix per $(\lambda/D)_{sky}$. There are a total of 1024 DM actuators (32x32 actuators) in the current 1-DM system, but we exclude the actuators with zero or very weak influences, thus reducing the number of the actuators used to <1024.

In this report, we carry out broadband control using three wavelengths: λ_1 = 770nm, λ_2 = 800nm, and λ_3 = 830nm. This is equivalent to simulating a broadband light with $\Delta\lambda/\lambda_0$ = 7.5%, where $\Delta\lambda$ is the bandwidth of the propagating beam and $\lambda_0=\lambda_2$. In this case, the e-field column-vector in Eqn. (2) is replaced with a broadband one as [8]

$$\vec{\mathbf{e}} = \begin{bmatrix} \vec{\mathbf{e}}(\lambda_1) \\ \vec{\mathbf{e}}(\lambda_2) \\ \vec{\mathbf{e}}(\lambda_3) \end{bmatrix}. \tag{5}$$

To obtain a broadband PSF, we calculate the PSF's at the above three individual wavelengths first, then take their arithmetic average with an equal weight.

3. CONTRAST PERFORMANCE OF FOUR PIAA CONFIGURATIONS

3.1 Schematic Diagrams of Four Different PIAA Coronagraph Configurations

In this section, we will compare the broadband contrast performance of four different PIAA coronagraph configurations. Their schematic diagrams are shown in Fig. 2, where the four configurations are identified as "C1" through "C4". Among them, C1 corresponds to the standard optical architecture currently being used on the HCIT in which the DM is placed downstream of the front end PIAA set and there is no an inverse-PIAA (iPIAA) at the back end of the optical system. C2 is the same as C1 except that the DM is placed upstream of the front end PIAA set. If we add an iPIAA set at the back end of C1 we obtain C3. Similarly, we obtain C4 by adding an iPIAA set to the back end of C2. In our simulations, the illumination of the DM covers approximately a 32-actuator diameter circle (out of 32x32 actuators).

The postapodizer used in the simulations of this section is a simple circular stop, not an annular binary postapodizer to be described later in this paper that is typically specified for PIAA coronagraphs. The occulter is the same as that explained in Sub-Section 2.2, and the Lyot stop is a circular aperture with $D_{\mathrm{lyo}}/D = 0.614$, where D and D_{lyo} are the diameters of the system clear aperture and the Lyot stop, respectively. As explained in Ref. 4, the PIAA mirrors apodize the pupil amplitude and distorts the phase map of the input pupil. At the same time, they produce a magnification and aberration of off-axis sources, which depends on the postapodizer and Lyot stop. For the four configurations explained above, this magnification is 2.5. For example, for C1 in Fig. 2, we have

$$(\lambda/D)_{\mathrm{sys}} = 2.5\times(\lambda/D)_{\mathrm{sky}}, \tag{6}$$

where the subscript "sys" means "system" and the $(\lambda/D)_{\mathrm{sys}}$ corresponds to the camera at the final focal plane.

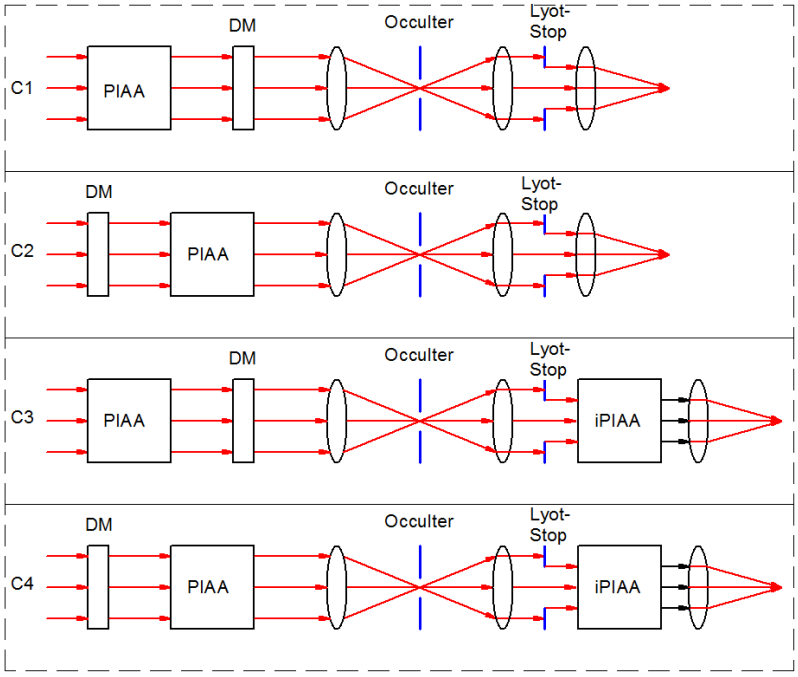

Fig.2. The schematic diagrams of four configurations, C1 through C4, to be simulated in this paper. Among them, C1 corresponds to the standard optical architecture currently in place on the HCIT in which the DM is placed downstream of the front end PIAA set and there is no an inverse-PIAA (iPIAA) at the back end of the optical system. C2 is the same as C1 except that the DM is placed upstream of the front end PIAA set. C3 is obtained by adding an iPIAA set at the back end of C1. Similarly, C4 is obtained by adding an iPIAA set to the back end of C2.

3.2 Broadband WFC: An Example

In this sub-section, we explain the process of our broadband WFC simulation with an example. If we apply the exit-pupil amplitude and phase of Figs. 1(a) and 1(b) to C1, and use a Lyot stop with $D_{\mathrm{lyo}}/D = 0.614$ as well as the occulter shown in Fig. 1(c), we obtain a broadband pre-control PSF as shown in Fig. 3(a), where the wavelength-dependent phase is modeled as $\phi = (2\pi/\lambda)\times OPD$, with the OPD given in Fig. 1(b). After carrying-out 15 iterations of broadband WFC, we obtain a broadband post-control PSF as shown in Fig. 3(b). The DM solutions which yield this result are shown in Fig. 3(c) as a DM actuator height map, and the normalized intensity I_{b} is shown as a function of control iteration number in Fig. 3(d). In this report, the broadband WFC for each simulation case is carried out with two γ_{wu} -values: With $\gamma_{\mathrm{wu}} = \gamma_{\mathrm{wu0}}$ for 5 iterations and with $\gamma_{\mathrm{wu}} = 10\times\gamma_{\mathrm{wu0}}$ for 10 iterations, where γ_{wu0} is an initial value of γ_{wu}. This γ_{wu0} is different for different configurations as well as for different input parameters. It also depends on how the sensitivity matrix $\tilde{\mathbf{S}}$ is calculated. Therefore, it needs to be determined by trial and error at the beginning of each simulation run. In the current example, a sharp decrease in I_{b} takes place when γ_{wu} transitions from γ_{wu0} to $10\times\gamma_{\mathrm{wu0}}$. This happens in many cases of our simulations, but not always.

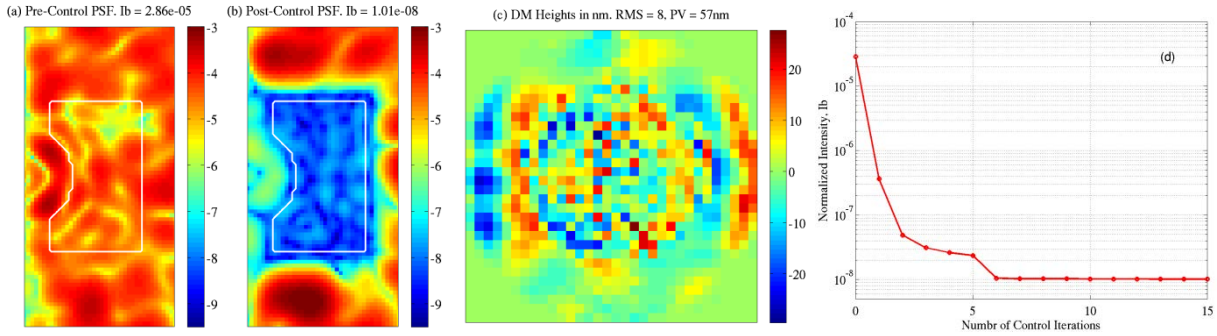

Fig.3. (a) Broadband PSF before wavefront control. It is obtained by averaging three PSF's at λ = 770, 800 and 830nm with an equal weight, where λ denotes the wavelength. (b) Broadband PSF after wavefront control. It is obtained in the same way as part (a) after carrying out WFC for 15 iterations with three wavelengths: 770, 800 and 830nm. (c) DM actuator heights used to obtain the PSF in part (b). (d) Normalized intensity, I_b, versus the number of control iterations. The WFC was carried in two steps: With $\gamma_{wu} = \gamma_{wu0}$ for 5 iterations and with $\gamma_{wu} = 10\times\gamma_{wu0}$ for 10 iterations, where γ_{wu0} is an initial value of γ_{wu}. In this case, a sharp decrease in I_b takes place after this transition.

3.3 Broadband Contrast of Four PIAA Configurations

In theory, placing a 32x32-actuator DM downstream of the front end PIAA sub-system allows one to control spatial-frequencies at most up to $16(\lambda/D)_{sys} = 6.4(\lambda/D)_{sky}$. On the other hand, if the DM is placed upstream of the front end PIAA sub-system, one will be able to control spatial-frequencies up to $16(\lambda/D)_{sky} = 40(\lambda/D)_{sys}$. We have evaluated the performance of the above four PIAA coronagraph configurations in terms of their OWA and broadband contrast for the two cases of exit-pupil phase: An idealized case of $\phi = 0$ and a realistic case of $\phi = \phi(\lambda) = (2\pi/\lambda)\times OPD$. The results of

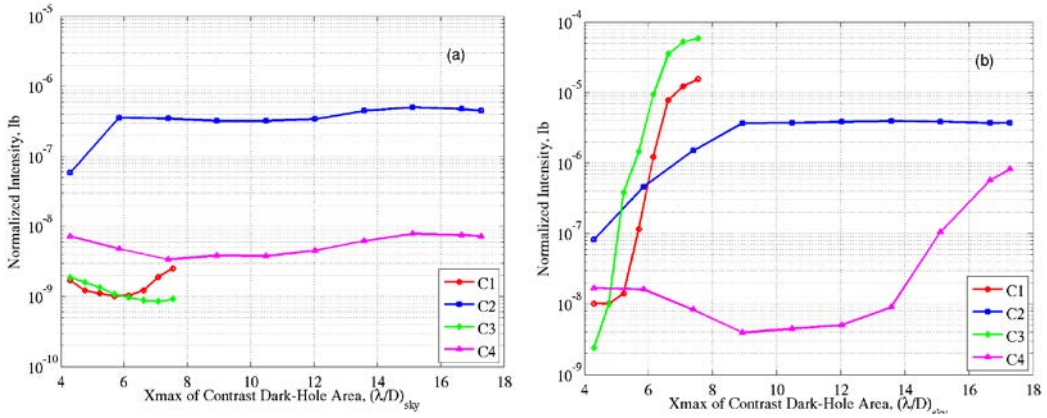

Fig.4. (a) Normalized intensity, I_b, versus X_{max} of the contrast dark-hole area when $\phi = 0$. The four different colors correspond to the four PIAA coronagraph configurations as indicated in the figure legends. The areas of both the control and the contrast dark-holes are increased by a variable ΔW in the form as $X_{max} = X_{max0} + \Delta W$, $Y_{max} = Y_{max0} + \Delta W$, and $Y_{min} = -Y_{max0} - \Delta W$, where the subscript "0" denotes the nominal value of the corresponding quantity. The other two dimensions, X_{min} and R_{min}, are kept unchanged. (b) Same as part (a), except $\phi = \phi(\lambda)$.

$\phi = 0$ are shown in Fig. 4(a), and those of $\phi = \phi(\lambda)$ are in Fig. 4(b), respectively. In these simulations, we increased the areas of both the control and the contrast dark-holes by a variable ΔW in the form as $X_{max} = X_{max0} + \Delta W$, $Y_{max} = Y_{max0} + \Delta W$, and $Y_{min} = -Y_{max0} - \Delta W$, where the subscript "0" denotes the nominal value of the corresponding quantity. The other two dimensions, X_{min} and R_{min}, are kept unchanged. In the idealized case, C1 and C3 work the best in terms of contrast, and C4 works the best in terms of OWA as expected. However, C2 does not work well. In the realistic case, C3 gives the best contrast at small OWA, and C4 does the same at large OWA. For C4, $I_b = 4.0\times10^{-9}$ at OWA = $X_{max} = 8.94(\lambda/D)_{sky}$. This value is $I_b = 3.9\times10^{-9}$ when $\phi = 0$. That is, C4 eliminates the effect of exit-pupil

phase error almost completely at some dark-hole areas. This was not expected before. Another important point to note is that C1 and C3 do not provide the expected control bandwidth (up to $6.4(\lambda/D)_{\text{sky}}$) when $\phi = \phi(\lambda)$. That is, in these two configurations, the phase error in the system reduces the size of the controllable area in the image plane. We will discuss this point further in the next section.

4. EFFECT OF EXIT-PUPIL PHASE ON CONTROL EFFICIENCY

In most active optical systems equipped with one or more DM's having a small number of actuators, say, for example, a few hundred actuators, the commonly used method for obtaining the sensitivity matrix $\widetilde{\mathbf{S}}$ is direct measurement. Indeed, it is a preferred method. The reason is that the resulted $\widetilde{\mathbf{S}}$ perfectly matches the optical system in which the wavefront sensing and control operations are to be performed. However, this method becomes unpractical for optical systems such as the HCIT, where the DM has 1024 actuators and measuring their e-field based influence functions is very time-consuming. Therefore, we obtain the $\widetilde{\mathbf{S}}$ used in both simulations and experiment from the model of the DM actuator and the HCIT optical system. One question we face in such a situation is what we should do with the exit-pupil phase, ϕ. In the real world the ϕ constantly changes due to drift and intentional motion of the optical hardware, and also as a result of a wavefront sensing and control process. It is not an easy task to re-calculate the $\widetilde{\mathbf{S}}$ for each new optical state. In all the simulations presented above, we used an $\widetilde{\mathbf{S}}$ matrix obtained with $\phi = 0$. In order to gain some understanding about the effect of this exit-pupil phase on the control efficiency of our testbed, we obtained a new set of $\widetilde{\mathbf{S}}$ including the $\phi = \phi(\lambda)$ shown in Fig. 1(b), and repeated the simulations of the several points in Fig. 4(a) for C1. The results are shown in Fig. 5(a), where we included the data of C1 shown in Figs. 4(a) and 4(b) for comparison. As we can see, matching the $\widetilde{\mathbf{S}}$ in terms of exit-pupil phase with the optical system to be controlled improves the control efficiency at regions where the OWA is small, but by very amount in the current case. This result suggests that we do not lose much by working with a phase-error-free $\widetilde{\mathbf{S}}$. As we pointed out in the previous section, the exit-pupil phase error not only raises the contrast floor we can achieve in a WFC process, but it also reduces the size of the image plane area that can be controlled. C1 is supposed to work up to $X_{\max} = 6.4(\lambda/D)_{\text{sky}}$ in its control dark-hole area, and indeed does so when $\phi = 0$. However, when $\phi = \phi(\lambda)$, the contrast floor starts to worsen as early as $X_{\max} \approx 5.2(\lambda/D)_{\text{sky}}$. Figure 5(b) shows the post-control PSF's of C1 when $X_{\max} = 6.2(\lambda/D)_{\text{sky}}$ in the range of $X = [0\ \ 6.96](\lambda/D)_{\text{sky}}$ and $Y = [-4.95\ \ 4.95](\lambda/D)_{\text{sky}}$.

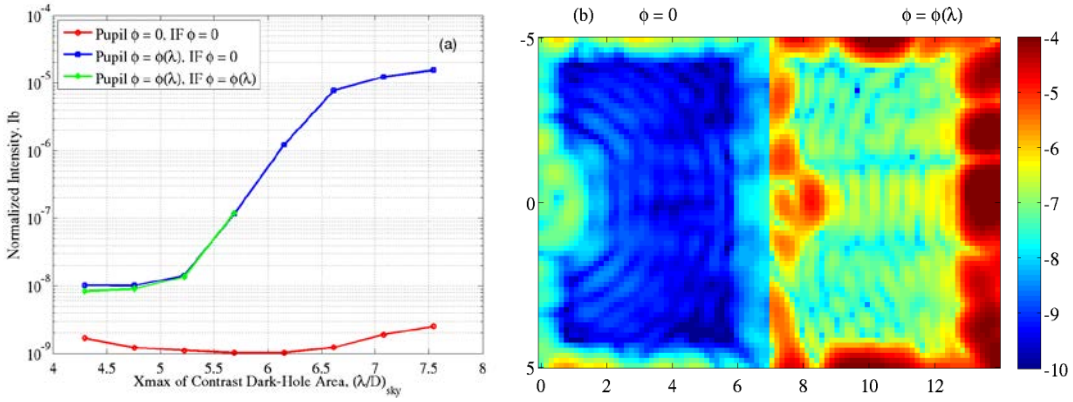

Fig.5. (a) Normalized intensity, I_b, versus $X_{\max}$ of the contrast dark-hole area for C1. The three different colors correspond to three different phase-error situations at the exit-pupil (Pupil ϕ) and when obtaining the sensitivity matrix (IF ϕ). The areas of both the control and the contrast dark-holes are increased by a variable ΔW in the form as $X_{\max} = X_{\max 0} + \Delta W$, $Y_{\max} = Y_{\max 0} + \Delta W$, and $Y_{\min} = -Y_{\max 0} - \Delta W$, where the subscript "0" denotes the nominal value of the corresponding quantity. The other two dimensions, $X_{\min}$ and $R_{\min}$, are kept unchanged. (b) Log-scale post-control PSF's corresponding to $X_{\max} = 6.2(\lambda/D)_{\text{sky}}$ in part (a). The units of the x- and the y-axes are $(\lambda/D)_{\text{sky}}$.

5. EFFECT OF DIFFERENT LYOT SIZES AND POSTAPODIZER DESIGNS

The current PIAA coronagraph testbed at JPL uses C1 as its optical configuration. Until now it has been operated with a narrow-band beam. The best narrow-band contrast achieved to date is $I_b \approx 5\text{x}10^{-10}$. In order to determine a "best" architecture for its broadband operation, we have investigated how C1 performs with a 7.5% broadband light and with various choices of postapodizer and Lyot stop size. In this section, we describe our simulation results.

5.1 Performance with a Designed PIAA Output Amplitude

The first part of this study was carried out with the designed PIAA output amplitude of Fig. 1(a). We considered three choices for a postapodizer: A circular stop, a 6-ring annular postapodizer, and a 10-ring annular postapodizer. If a circular-stop postapodizer is applied after the PIAA mirrors, the coronagraph produces an amplitude at the exit-pupil of Fig. 1(a), seen through the entire system with no occulter and Lyot stop. The same amplitude produced with a 6-ring annular postapodizer is shown in Fig. 6(a). If the coronagraph is free of phase error, then the amplitude of Fig. 1(a) produces a PSF as shown in Fig. 6(b), and that of Fig. 6(a) produces a PSF in Fig. 6(c). That is, in this case, the net effect of the 6-ring postapodizer is to produce an annular dark-hole from $R_{\min} \approx 2(\lambda / D)_{\text{sky}}$ to $R_{\max} \approx 4(\lambda / D)_{\text{sky}}$. The similar results obtained with a 10-ring postapodizers are shown in Figs. 6(d) and 6(f). Figs. 6(b) and 6(e) are the same except that Fig. 6(e) shows a larger area of the PSF than in Fig. 6(b). In this case, the 10-ring annular postapodizer creates an annular dark-hole from $R_{\min} \approx 2(\lambda / D)_{\text{sky}}$ to $R_{\max} \approx 8(\lambda / D)_{\text{sky}}$ with a contrast floor comparable to that of 6-ring postapodizer.

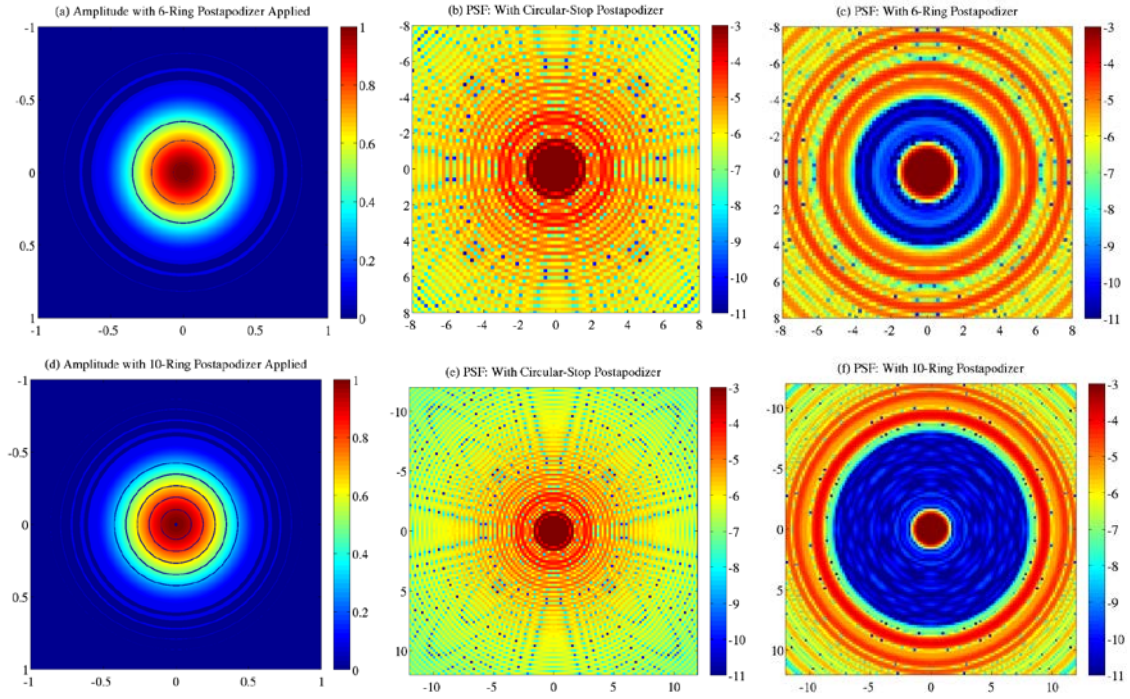

Fig.6. Exit-pupil amplitude and PSF maps obtained in C1 with $\phi = 0$. (a) Exit-pupil amplitude when a 6-ring postapodizer is used. (b) Pre-control PSF obtained with a circular-stop postapodizer. The corresponding pupil amplitude is the same as that in Fig. 1(a). (c) Pre-control PSF obtained with the 6-ring postapodizer of part (a). (d) Exit-pupil amplitude when a 10-ring postapodizer is used. (e) Same as part (b) except that its area is matched with part (f). (f) Pre-control PSF obtained with the 10-ring postapodizer of part (d).

The real coronagraph system is not free of phase-error. As a result, the two annular ring postapodizers cannot produce an annular dark-hole region in their own, and one needs to perform WFC to generate dark-holes. In order to take advantage of the function of the 6-ring and the 10-ring postapodizers, we carry out our following simulations with a new, semi-annular dark-hole region. That is, we use $[X_{\min}, R_{\min}, R_{\max}] = [0.75, 1.72, 4.83](\lambda / D)_{\text{sky}}$ for control dark-hole, and $[X_{\min}, R_{\min}, R_{\max}] = [1.07, 2.04, 4.50](\lambda / D)_{\text{sky}}$ for contrast dark-hole, respectively. Figure 7(a) shows the normalized

intensity I_b as a function of normalized Lyot-stop diameter, D_{lyo}/D. The last data points at $D_{lyo}/D = 1.15$ correspond to a case where the Lyot-stop is removed. In the case of a circular-stop postapodizer, the I_b decreases first, then increases, reaching an optimum value at $D_{lyo}/D \approx 0.75$. It exhibits somewhat irregular behavior with the 6-ring postapodizer, and gets the best value of $I_b = 2.6\times10^{-9}$ at $D_{lyo}/D = 1.05$ among all cases considered. The 10-ring postapodizer produces the most interesting I_b result. That is, the I_b becomes smaller with increased D_{lyo}/D and reaches an optimum value when the Lyot-stop is removed. We believe the observed the behavior of the I_b is dependent on the residual phase error included in these simulations and may change if the optical system has a different set of phase error.

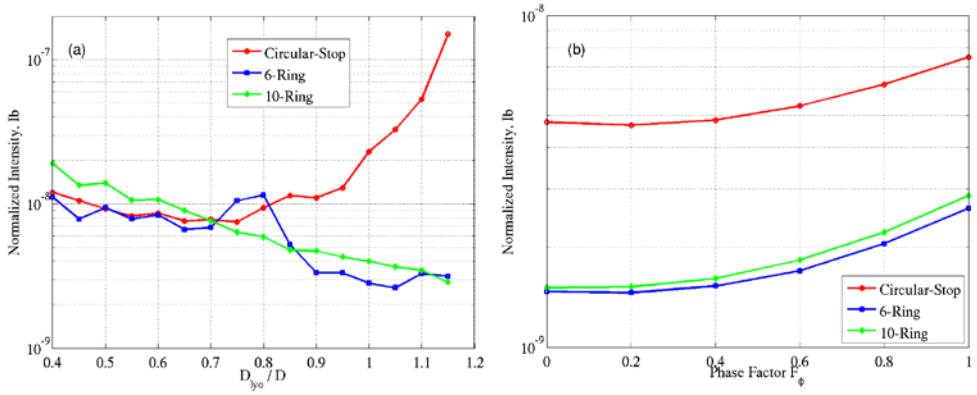

Fig.7. (a) Normalized intensity, I_b, versus D_{lyo}/D for C1. The three different colors correspond to circular-stop, 6-ring and 10-ring postapodizers, respectively. The last data points at $D_{lyo}/D = 1.15$ are obtained without Lyot stop, or with $D_{lyo}/D = \infty$. (b) Normalized intensity, I_b, versus phase scaling factor, F_ϕ. In this part, the I_b is evaluated with a series of new exit-pupil phase errors given by $\phi = F_\phi\phi(\lambda)$ and by setting D_{lyo}/D to its optimum values: $D_{lyo}/D = 0.75$ for circular-stop, $D_{lyo}/D = 1.05$ for 6-ring, and $D_{lyo}/D = \infty$ for 10-ring postapodizers, respectively.

In order to get an understanding on how much improvement we can get in I_b if we reduce the exit-pupil residual phase error, we evaluated the I_b by changing the exit-pupil phase error as $\phi = F_\phi\phi(\lambda)$, and by setting D_{lyo}/D to its optimum values: $D_{lyo}/D = 0.75$ for circular-stop, $D_{lyo}/D = 1.05$ for 6-ring, and $D_{lyo}/D = \infty$ for 10-ring postapodizers, respectively. The results of I_b are shown as a function of F_ϕ in Fig. 7(b). The 6-ring postapodizer maintains its leading performance in the entire range of F_ϕ, and gives a best result of $I_b = 1.5\times10^{-9}$ at $F_\phi = 0$.

We found that the DM actuator displacement is quite different for three postapodizers. In Figs. 8(a-i) we show the pre-control PSF, post-control PSF, and the corresponding DM actuator heights obtained in C1 with the three different postapodizers: Circular-stop (top-row), 6-ring (middle-row), and 10-ring (bottom-row) postapodizers, respectively. We used $D_{lyo}/D = 0.7$ here because the three postapodizers produce comparable I_b results at this D_{lyo}/D value. The area of the active actuators is the largest with the circular-stop postapodizer, and the smallest with the 10-ring postapodizer. The root-mean-square (RMP) and the peak-to-valley (PV) values of the DM actuator heights are also the smallest in the latter case. That is, to achieve the same contrast level, one utilizes the DM actuators the less when using a 10-ring postapodizer than one does with a circular-stop postapodizer. The behavior of the DM actuators when using a 6-ring postapodizer falls in between those of the circular-stop and the 10-ring postapodizers.

We also want to know the best expected performance of the current PIAA coronagraph testbed when a different postapodizer is used. To this end, we repeated the I_b versus D_{lyo}/D simulations with the measured amplitude at the exit-pupil shown in Fig. 9(a). Figure 9(b) shows the corresponding normalized intensity results. Again, the 6-ring postapodizer performs the best, but the best contrast value never reaches to $1\text{x}10^{-8}$.

There can be a mismatch between the front end PIAA mirrors output and the postapodizer due to some design and/or fabrication errors. In order to understand how much impact such an error has on the broadband contrast, we varied the

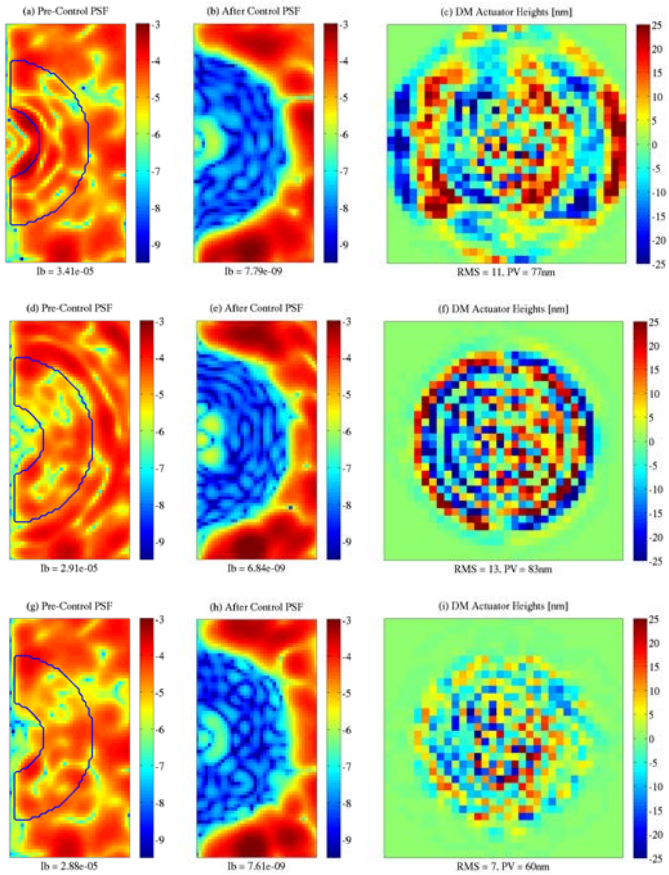

Fig.8. Pre-control PSF, post-control PSF and the corresponding DM solutions obtained with a circular-stop (top row), a 6-ring (middle-row) and a 10-ring (bottom-row) postapodizers, respectively. $D_{\text{lyo}} / D = 0.7$ in all cases. The blue frames in pats (a), (d) and (g) show the area of contrast dark-hole. The x-labels of parts (c), (f) and (i) are the root-mean-square (RMS) and the peak-to-valley (PV) values of the corresponding DM actuator height maps.

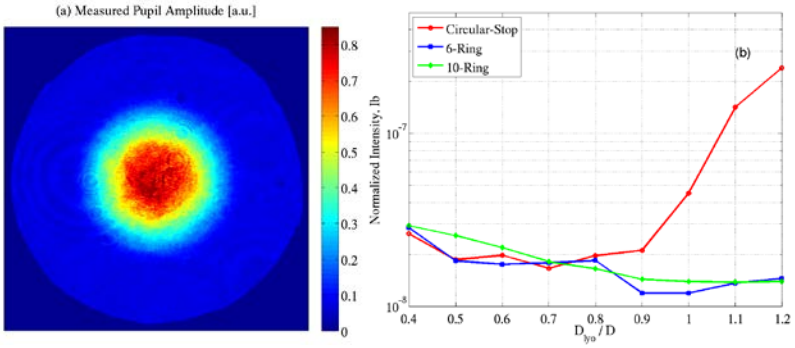

Fig.9. (a) Estimated amplitude at the exit-pupil, seen through the entire coronagraph with no occulter and Lyot stop. It is displayed in a linear scale. The upper-limit of its color-stretch is reduced from 1.0 to 0.85 for better visualization of its fine details. The amplitude at the edge is approximately 1/10 that at the center. (b) Normalized intensity, I_b, versus D_{lyo} / D for C1. The three different colors correspond to circular-stop, 6-ring and 10-ring postapodizers, respectively. The last data points at $D_{\text{lyo}} / D = 1.2$ correspond to no Lyot-stop, or $D_{\text{lyo}} / D = \infty$.

radius of the annular transparent and opaque bands of the 6-ring postapodizer as $T = T(F_r r)$, and evaluated the broadband contrast of C1 for three values of F_r, F_r =0.97, 1.00 and 1.03. Figure 10(Left) shows the profile of the

designed PIAA output amplitude with the three 6-ring annular postapodizer, and Fig. 10(Right) shows corresponding normalized intensity map after control. The I_b–value of each case is given in the x-label of the same plot. The I_b–value increases by a factor of 1.69 and 1.73 when F_r = 0.97 and 1.03, respectively. For the above three values of F_r, we got $I_b = 1.2\times10^{-8}, 1.2\times10^{-8}$ and 1.5×10^{-8}, respectively, when we used the measured pupil amplitude instead.

Another possible situation regarding the alignment of a postapodizer with the PIAA mirrors is the off-centering of the postapodizer relative to the PIAA output. In order to gain some quantitative understanding on the impact of such a situation on the broadband contrast, we off-centered the 6-ring postapodizer up to $\Delta x/D = \pm 0.05$ along the x-axis, and by the same amount along the y-axis, along one direction at a time, and evaluated the corresponding before- and after-control I_b-values. Figure 11(a) shows the PIAA output amplitude profile when $\Delta x/D$ = -0.05, 0 and 0.05, and Fig. 11(b) shows the before-control (solid-curves) and after-control (dashed-curves) I_b-values obtained with the design PIAA output amplitude for C1. We have the capability on the current testbed to align a postapodizer with a sub-micron precision, and we believe the above sensitivity of the HCIT contrast on the postapodizer position is good enough for us to position a postapodizer with a fairly high accuracy.

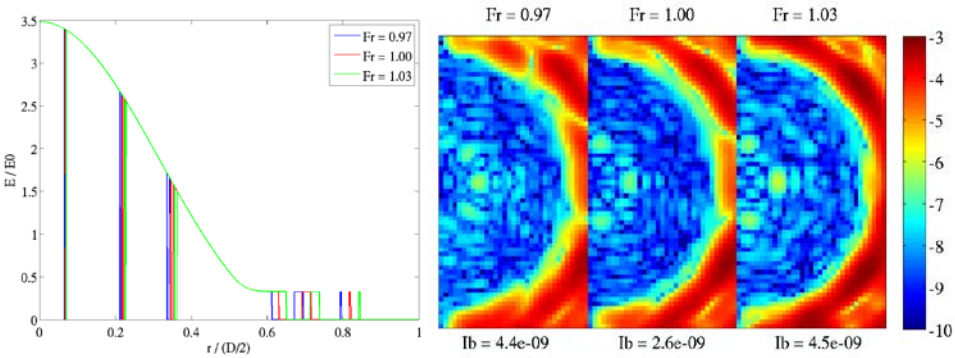

Fig.10. (Left) Cross-section of the design PIAA output amplitude with a 6-ring annular postapodizer whose transmittance is defined by $T = T(F_r r)$, where r is a radial position variable and F_r is a scaling factor. (Right) Normalized after-control PSF's corresponding to three F_r–values: F_r = 0.97, 1.00, and 1.03. The corresponding mean normalized intensity inside the dark-hole, I_b, is shown in the x-label.

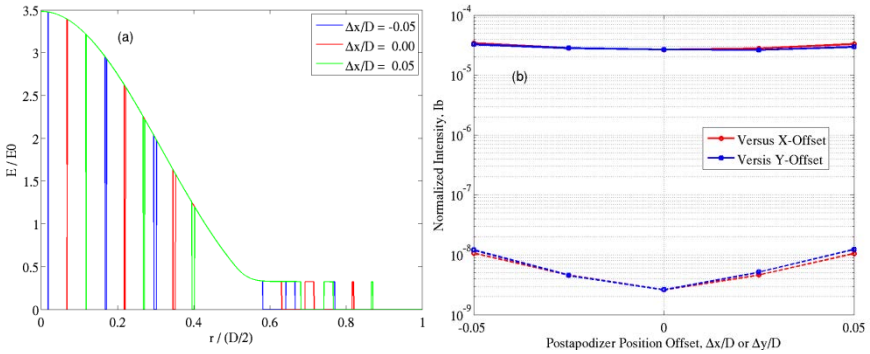

Fig.11. (a) Cross-section of the design PIAA output amplitude with a 6-ring annular postapodizer off-centered in the x-direction by $\Delta x/D$ =-0.05, 0 and 0.05. (b) Before-control (solid-curves) and after-control (dashed-curves) I_b–values of C1 corresponding to different 6-ring postapodizer de-centering values. The postapodizer was de-centered in only one direction at a time.

6. CONCLUSION

One of the important milestones of the PIAA coronagraph project is to demonstrate 1×10^{-9} contrast with 10% bandwidth. In order to identify the potentials and the limitations of the current single-DM PIAA coronagraph on HCIT, we have evaluated through modeling and simulations the broadband contrast performance of four different PIAA

coronagraph configurations. The simulation results confirmed that an inverse-PIAA expands the OWA. A somewhat surprising result is that, at some dark-hole size, the inverse-PIAA also improves the control efficiency, yielding better broadband contrast values as compared to the corresponding no inverse-PIAA case. Overall, the C4 performs the best with the designed PIAA output amplitude in terms of both broadband contrast and OWA. For C1, the optimum Lyot stop size is different for different postapodizer designs, and the 10-ring annular postapodizer performs the best when the Lyot stop is completely removed. Different postapodizer designs require different DM actuator displacements to achieve comparable contrast levels. Our simulations predicted that the best 7.5%-broadband contrast achievable with C1, the designed PIAA output amplitude and the 6-ring annular postapodizer is 2.6×10^{-9}. This result degrades to 1.5×10^{-8} if the amplitude estimated at the exit-pupil of the current system is used. The sensitivity of C1's contrast performance to the PIAA-postapodizer mismatch and to the postapodizer position error was also investigated. It was found that a 3% mismatch between the 6-ring postapodizer and the PIAA output worsens the contrast level up to a factor of ~1.7. It was shown that the sensitivity of the pre-control and the post-control contrast values to the lateral position of a postapodizer can be used to align it with the PIAA output with a satisfactory accuracy within our current capability. We believe the above findings are very useful in determining the future direction of this project.

ACKNOWLEDGEMENTS

This work was carried out at the Jet Propulsion Laboratory, California Institute of Technology, under contract with the National Aeronautics and Space Administration.

REFERENCES

1. Guyon, O. et al., "High-contrast imaging and wavefront control with a PIAA coronograph: Laboratory system validation,", Pub. Astron. Soc. Pacific 122, 71-84 (2010).
2. Guyon O. et al., "Phase induced amplitude apodization (PIAA) coronagraphy: recent results and future prospects," *Proc. SPIE*, **8151**, 81510H (2011).
3. Guyon O. et al., "Phase induced amplitude apodization (PIAA) coronagraphy: recent results and future prospects," *Proc. SPIE*, **8442**, 84424V (2012).
4. Kern, B. et al., "Phase-induced amplitude apodization (PIAA) coronagraph testing at the High Contrast Imaging Testbed," *Proc. SPIE*, **7440**, 7440H (2009).
5. Kern, B. et al., "Laboratory testing of a Phase Induced Amplitude Apodization (PIAA) coronagraph," *Proc. SPIE*, **8151**, 815104 (2011).
6. Erkin Sidick, Stuart Shaklan, and Kunjithapatham Balasubramanian, "HCIT broadband contrast performance sensitivity studies," *Proc. SPIE,* **8520**, pp.85200M (2012).
7. Erkin Sidick, Scott A. Basinger, and David C. Redding, "An improved wavefront control algorithm for large space telescopes," *Proc. SPIE*, **7015**, 70154P (2008).
8. Amir Give'on *et al.*, "Broadband wavefront correction algorithm for high-contrast imaging system," *Proc. SPIE*, **6691**, 66910A (2007).